

Article

# High-Efficiency All-Dielectric Metasurfaces for the Generation and Detection of Focused Optical Vortex for the Ultraviolet Domain

Ziheng Zhang <sup>1,2,3</sup>, Tong Li <sup>4</sup>, Xiaofei Jiao <sup>1,2,3</sup>, Guofeng Song <sup>1,2,3,\*</sup> and Yun Xu <sup>1,2,3</sup>

<sup>1</sup> Institute of Semiconductors, Chinese Academy of Sciences, Beijing 100083, China; zhzheng92@semi.ac.cn (Z.Z.); xfjiao@semi.ac.cn (X.J.); xuyun@semi.ac.cn (Y.X.)

<sup>2</sup> College of Materials Science and Opto-Electronic Technology, University of Chinese Academy of Sciences, Beijing 100049, China

<sup>3</sup> Beijing Key Laboratory of Inorganic Stretchable and Flexible Information Technology, Beijing 100083, China

<sup>4</sup> School of Physics and Electronic Sciences, Changsha University of Science and Technology, Changsha 410004, China; lt@csust.edu.cn

\* Correspondence: sgf@semi.ac.cn

Received: 30 July 2020; Accepted: 17 August 2020; Published: 18 August 2020



**Featured Application:** Optics and Lasers, Integrated Ultraviolet Nanophotonics, Meta-optics.

**Abstract:** The optical vortex (OV) has drawn considerable attention owing to its tremendous advanced applications, such as optical communication, quantum entanglement, and on-chip detectors. However, traditional OV generators suffer from a bulky configuration and limited performance, especially in the ultraviolet range. In this paper, we utilize a large bandgap dielectric material, niobium pentoxide ( $\text{Nb}_2\text{O}_5$ ), to construct ultra-thin and compact transmission-type metasurfaces to generate and detect the OV at a wavelength of 355 nm. The meta-atom, which operates as a miniature half-wave plate and demonstrates a large tolerance to fabrication error, manipulates the phase of an incident right-handed circular polarized wave with high cross-polarized conversion efficiency (around 86.9%). The phase delay of  $\pi$  between the orthogonal electric field component is attributed to the anti-parallel magnetic dipoles induced in the nanobar. Besides, focused vortex generation (topological charge  $l$  from 1 to 3) and multichannel detection ( $l$  from  $-2$  to 2) are demonstrated with high efficiency, up to 79.2%. We envision that our devices of high flexibility may have potential applications in high-performance micron-scale integrated ultraviolet nanophotonics and meta-optics.

**Keywords:** dielectric metasurface; polarization conversion; optical vortex; niobium pentoxide

## 1. Introduction

The optical vortex (OV), characterized by a donut intensity distribution and a helically structured wavefront, shows a phase evolution in the form of  $e^{il\theta}$ , where  $\theta$  is the azimuthal angle and  $l$  is the topological charge. It has aroused significant scientific curiosity since its discovery in 1992 [1] and produced tremendous applications in the field of optical tweezers [2], optical communication [3], quantum entanglement [4], nanotechnology [5], biomedicine [6], on-chip detectors [7], etc. Nevertheless, conventional OV generators, such as spiral phase plates [8], axicon lenses [9], and pitch fork holograms [10], suffer from limited performance, bulky configurations, and difficulty of integration. Therefore, it is of great urgency to seek miniaturized devices for OV generation and detection, and metasurfaces seem a promising candidate.

A metasurface, composed of arrays of sub-wavelength nanostructures, is a two-dimensional (2D) analog of metamaterials. It can manipulate the phase, polarization, and amplitude of electromagnetic

waves flexibly at the nanoscale, making the integration and planarization of traditional bulky optical devices possible. It has an inspiringly diverse range of applications in areas such as beam steering [11], polarization conversion [12], holography [13,14], perfect absorption [15], self-accelerating beams [16], flat lenses [17,18], etc. The metallic reflective metasurface based on gap plasmons can achieve an efficiency of around 80% in the near-infrared and visible ranges [14]. However, most optical devices work in transmission mode. Due to the inherent ohmic losses, the transmissive metallic metasurfaces suffer from low efficiency. However, low-loss dielectric metasurfaces based on magnetic resonance demonstrate large transmittance, illustrating the potential to become a strong competitor of the metallic metasurface. Lead telluride (PbTe)-based metasurfaces [19] and gallium antimonide (GaSb)-based metasurfaces [20] have an efficiency of over 70% in the mid-infrared range, and silicon (Si) metasurfaces [21] achieve an efficiency of around 90% in the near-infrared range. Moreover, dielectric materials such as titanium dioxide (TiO<sub>2</sub>) [22], gallium nitride (GaN) [23], silicon nitride (Si<sub>3</sub>N<sub>4</sub>) [24], and other high-refractive-index, low-loss materials have also illustrated remarkable performance, with over 70% efficiency in the visible range.

However, the materials discussed above render relatively low transmission efficiency in the ultraviolet (UV) range. Furthermore, UV-transparent materials such as CaF<sub>2</sub>, MgF<sub>2</sub>, and SiO<sub>2</sub> have relatively low refractive indices, making design and fabrication significantly challenging. Deng experimentally demonstrated all-silicon-based broadband UV metasurfaces operating efficiently at wavelengths down to 290 nm. Nonetheless, the device suffered from a low efficiency of under 30% [25]. Zhang illustrated a high-performance, complementary metal oxide semiconductor (CMOS) compatible hafnium oxide (HfO<sub>2</sub>)-based metasurface working at wavelengths down to a record short deep-UV range [26]. Nevertheless, the aspect ratio of the nanobar was larger than 10, thus adding strict requirements for preparation. Gao designed aluminum nitride (AlN)-based multi-plane meta-holography by adopting circular posts with different diameters at an efficiency of 34.05% [27]. However, the abrupt phase difference formed by the nano-cylinder changed rapidly within a specific range of the cylinder radius, giving little tolerance to manufacturing error. In summary, the ultraviolet metasurface faces three major problems: low efficiency, large aspect ratio, and low fabrication error tolerance.

Consequently, we design a niobium pentoxide (Nb<sub>2</sub>O<sub>5</sub>)-based transmission-type all-dielectric metasurface to address the challenges discussed above. Nb<sub>2</sub>O<sub>5</sub>, with a bandgap of about 3.65 eV, exhibits a wide transparency window covering the ultraviolet, visible, and infrared regions [28]. Additionally, Nb<sub>2</sub>O<sub>5</sub> also has excellent mechanical strength [29], chemical stability, high permittivity, and low absorption [28]. These attractive characteristics enable multiple applications in solar cells, light-emitting diodes, sensing devices, catalysts, electrochromic devices, etc. [28]. Moreover, numerous studies have reported Nb<sub>2</sub>O<sub>5</sub> film manufacturing strategies and the synthesis methodology of Nb<sub>2</sub>O<sub>5</sub> nanostructures [28]. These advantages discussed above make Nb<sub>2</sub>O<sub>5</sub> a promising material in the ultraviolet range.

In this paper, we design meta-atoms composed of Nb<sub>2</sub>O<sub>5</sub> nanobars on silica substrate. The meta-atom operates as a miniature half-wave plate and shows a large tolerance for fabrication error. The orientation–rotation angle of the nanobar is varied to attain the complete  $2\pi$  phase control of incident right-handed circular polarization (RCP) waves with high cross-polarized transmission efficiency in the ultraviolet range. In addition, we discuss the optically induced anti-parallel magnetic dipoles (AMDs) holding the underlying physics of the  $\pi$  phase delay in the meta-atom. Moreover, we illustrate high-performance dielectric metasurfaces for the generation of a focused optical vortex in the UV range with a maximum efficiency of over 79%. Additionally, multichannel topological charge resolved devices based on multi-wave interference are demonstrated with detection of the topological charges from  $-2$  to  $2$ . Larger topological charges of the optical vortex can be generated and detected if the metasurface is big enough. Our devices of high flexibility may have potential applications in high-performance micron-scale integrated ultraviolet nanophotonics and meta-optics.

## 2. Theory and Meta-Atom Design

Depending on the geometry, a high refractive indexed meta-atom with sufficient height can manipulate the phase, polarization, and amplitude of the incident electromagnetic wave. Figure 1a shows the sketch of the proposed meta-atom. A Nb<sub>2</sub>O<sub>5</sub> nanobar with an orientation-rotating angle  $\theta$  is patterned on a silica substrate to obtain the desired phase manipulation. As the nanostructure in the designed meta-atom is a simple rectangular nanobar, the transmission coefficients of this structure can be represented using the Jones matrix [30]:

$$\hat{t}(\theta) = \begin{bmatrix} t_x \cos^2 \theta + t_y \sin^2 \theta & (t_x - t_y) \sin \theta \cos \theta \\ (t_x - t_y) \sin \theta \cos \theta & t_y \cos^2 \theta + t_x \sin^2 \theta \end{bmatrix} \quad (1)$$

where  $t_x$  and  $t_y$  are the complex transmission coefficients when the polarization of an incident wave is  $x$ -polarized and  $y$ -polarized, respectively. Given the right-handed circular-polarized (RCP) light ( $E_i = (\hat{e}_x + i\hat{e}_y) / \sqrt{2}$ ) of incidence, the transmitted electric field  $E_t$  can be written as follows [31]:

$$E_t = \hat{t}(\theta) \bullet E_i = \frac{t_x + t_y}{2} E_{RCP} + \frac{t_x - t_y}{2} e^{i2\theta} E_{LCP} \quad (2)$$

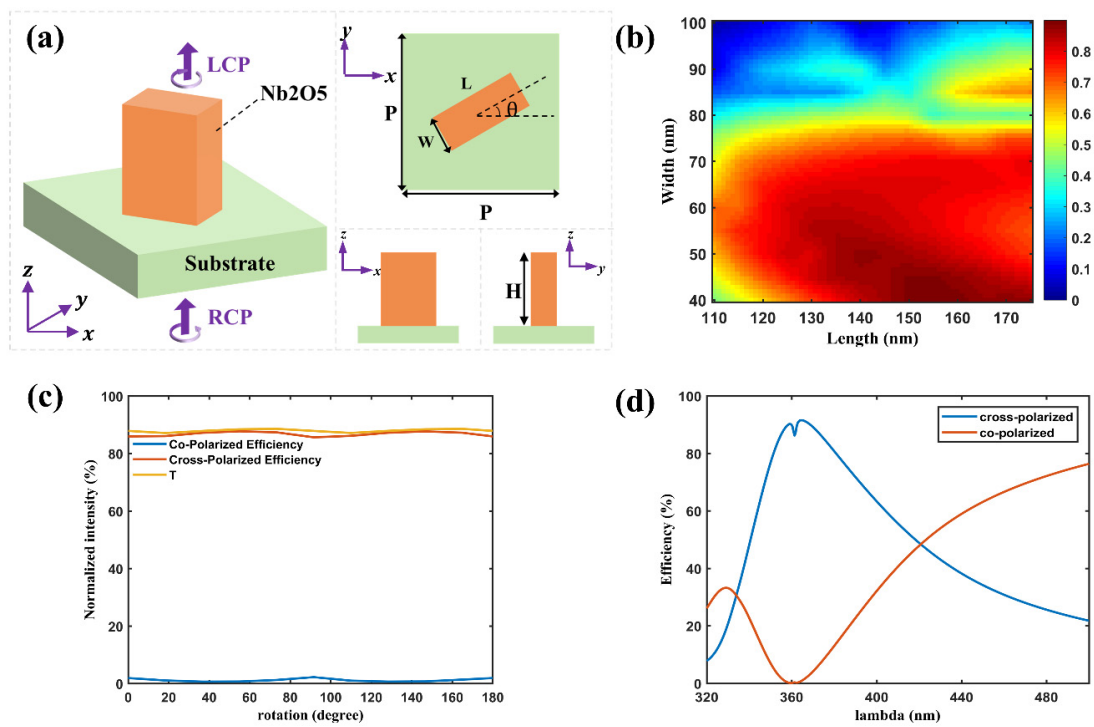


**Figure 1.** The optical properties of the Nb<sub>2</sub>O<sub>5</sub>-based meta-atom. (a) Sketch of the Nb<sub>2</sub>O<sub>5</sub> nanobar with a rotation angle of  $\theta$  on the silica substrate. This meta-atom is designed to convert the incident right-handed circular polarization (RCP) plane wave into the transmitted left-handed circular polarization (LCP) wave with an additional phase modulation of  $e^{i2\theta}$ . (b) Simulated conversion efficiency  $\eta$  for the nanobar with optimized height  $H = 340$  nm, period  $P = 200$  nm, and various lengths  $L$  and widths  $W$  under the RCP wave incidence at 355 nm. (c) The transmission (orange line), co-polarized (RCP, blue line), and cross-polarized (LCP, red line) efficiencies versus rotation angle  $\theta$  of the Nb<sub>2</sub>O<sub>5</sub> nanobar arrays under the RCP wave incidence at 355 nm. (d) The transmitted co-polarized and cross-polarized efficiencies of the optimized meta-atom arrays are investigated within a broadband wavelength range.

The first term in Equation (2) represents a co-polarized transmitted wave component with the same helicity as the incident light. The second term represents a cross-polarized transmitted wave with the opposite helicity and an additional Pancharatnam–Berry (PB) phase manipulation of  $e^{i2\theta}$ . Therefore, through rotating the anisotropic nanobar from 0 to  $\pi$ , the full  $2\pi$  phase shift of the transmitted cross-polarized wave component can be achieved.

The meta-atom is under the incidence of the RCP plane wave at a wavelength at 355 nm. The simulation of the structure is implemented by using the finite-difference time-domain (FDTD) method through the commercial software Lumerical FDTD. The computational area is set to be  $200 \times 200 \times 200$  nm in the  $x$ ,  $y$ , and  $z$  directions, respectively. Periodic boundary conditions are used in the  $x$  and  $y$  directions of a unit cell. In contrast, the perfectly matched layer (PML) boundaries are applied along the  $z$  direction to eliminate unwanted reflections. The optical constant of niobium pentoxide is taken from F. Lemarchand's report [32], and the optical constant of the silica substrate is taken from the work of Palik [33]. The length ( $L$ ) and width ( $W$ ) are swept to maintain a high cross-polarized efficiency, which is defined as the ratio of the transmitted light with cross-polarization to the total incident light. Figure 1b shows the simulated efficiency changes with the length ( $L$ ) varying from 110 to 170 nm and the width ( $W$ ) from 40 to 100 nm. The height ( $H$ ) of the nanobar and the period ( $P$ ) of the square meta-atom are fixed to the optimized values of 340 nm and 200 nm, respectively. The peak efficiency of 86.9% is achieved with  $L = 165$  nm and  $W = 45$  nm, and the adjacent geometries also exhibit efficiencies over 80%, thus resulting in a relatively large tolerance to fabrication error. Figure 1c shows that the transmission ( $T$ ), co-polarized, and cross-polarized efficiencies remain uniform as the  $\text{Nb}_2\text{O}_5$  nanobar is rotated from 0 to  $\pi$ . Figure 1d illustrates the simulated broadband analysis of an optimized nanobar in the range of 320 nm to 500 nm. The efficiency of the cross-polarized component is over 80% around the working wavelength of 355 nm. Moreover, there is a gradual increase in the transmission of the meta-atom, which implies that this  $\text{Nb}_2\text{O}_5$ -based nanostructure with an optimized geometry could gain high efficiency in the visible range.

The high conversion efficiency of the meta-atom requires two conditions: a high transmission of both electric fields and a phase delay of  $\pi$  between the orthogonal electric field components, in other words, the meta-atom should operate as a high-performance miniature half-wave plate. It has been reported that in dielectric metasurfaces, the displacement current and its induced magnetic field produced both electric and magnetic resonance in the nanostructure, resulting in a high transmission efficiency [34]. Besides, the complex refractive index of  $\text{Nb}_2\text{O}_5$  has a sufficiently larger real part with a low extinction coefficient. This also contributes to the high efficiency of transmission. The phase delay of  $\pi$  can be attributed to the existing antiferromagnetic resonance mode in the structure [35]. For a better understanding of the physical mechanism behind the phase delay of  $\pi$ , the vector field orientations and cross-sectional intensities of electric and magnetic fields for an optimized nanobar are plotted in Figure 2 under the incidence of a plane wave at 355 nm. As is demonstrated in Figure 2a,b, for the  $x$ -polarized incident wave, four circle displacement currents with the alternate direction of rotation induce four AMDs vertically located along the  $z$ -axis. The induced AMDs are staggered in anti-parallel orientations. This even number of displacement currents keeps the electric vectors of the incident and transmitted wave in the same direction. Figure 2c shows the simplified sketches of this antiferromagnetic mode under an  $x$ -polarized wave incidence. In contrast, the  $y$ -polarized incident wave induces three AMDs vertically located along the  $z$ -axis, resulting in the electric vector of the transmitted light being inverse to that of incident light (see Figure 2d–f). Thus, the transmitted electric vectors of  $x$ - and  $y$ -polarized components are in the opposite direction, introducing a phase delay of  $\pi$ .

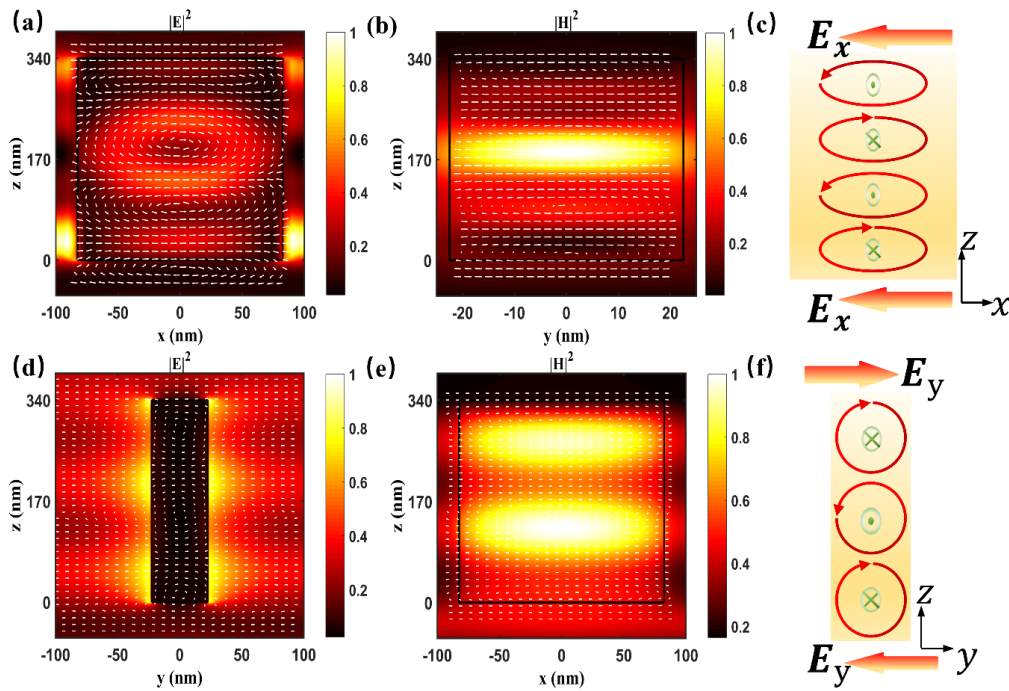


**Figure 2.** Excitation of anti-parallel magnetic dipoles (AMDs) in a Nb<sub>2</sub>O<sub>5</sub> nanobar. (a,d) Normalized total electric ( $|E|^2$ ) fields and (b,e) normalized total magnetic ( $|H|^2$ ) field existing in the optimized nanobar under 355 nm  $x$ - and  $y$ -polarized wave incidence, respectively. The white arrows denote the induced corresponding field's vector profiles in and near the nanobar, and the black lines distinguish the boundaries of the nanobar. Simplified sketches of excited antiferromagnetic modes with even and odd dipoles are shown in (c) and (f), respectively.

### 3. Results and Discussion

#### 3.1. Focused Optical Vortex Generation

A succinct view of the designed transmission-type focused optical vortex (FOV) generator is presented in Figure 3a, the device combines the functions of a lens and a spiral phase plate into a single metasurface. The phase distribution profile of the FOV generator can be divided into the optical vortex profile  $\varphi_{OV}$  and lens profile  $\varphi_{lens}$ . Thus, the expression for the phase profile can be written as follows:

$$\begin{aligned} \phi_m(x, y) &= \varphi_{OV} + \varphi_{lens} \\ &= l * \arctan\left(\frac{y}{x}\right) - \frac{2\pi}{\lambda} \left( \sqrt{x^2 + y^2 + f^2} - f \right) \end{aligned} \quad (3)$$

where  $\lambda$  is the design wavelength (here  $\lambda = 355$  nm),  $f$  is the focal length,  $l$  is the topological charge, which defines the degree of helicity at the focal point, while  $x$  and  $y$  are the transverse coordinates on the metasurface plane. Then we can obtain the spatial distribution of the phase profile compensated by the metasurface through adjusting the rotation angle  $\theta_x, y$  of the optimized Nb<sub>2</sub>O<sub>5</sub> nanobars discussed above, where  $\theta(x, y) = \phi_m(x, y)/2$ .

$$NA = \sin(\phi) = \frac{D}{\sqrt{4f^2 + D^2}}. \quad (4)$$

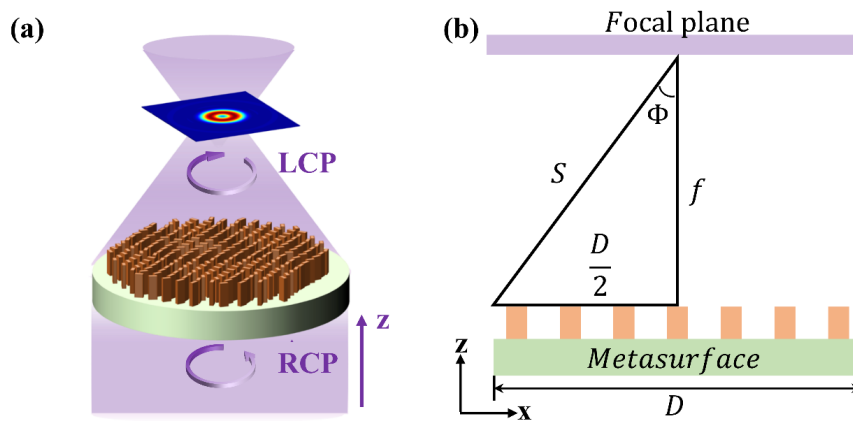


**Figure 3.** (a) Sketch of a transmission-type focused optical vortex (FOV) generator under the RCP incidence. The LCP transmissive wave with the desired topological charge can be observed with a donut-shaped ring in the middle of the focal plane. (b) Demonstration of numerical aperture (NA) calculation for the FOV generator.

The calculation for numerical aperture (NA) is displayed in Figure 3b and Equation (4). Here,  $D$  is the diameter of the metasurface and  $s$  is the hypotenuse of the right triangle. The diameter of the metasurface is kept at  $12\ \mu\text{m}$  to achieve a NA of 0.514.

A full-wave numerical simulation of all the designed FOV generators is calculated through FDTD methods. PML boundary conditions are applied along all the  $x$ ,  $y$ , and  $z$  axes, and the incidence is the RCP plane wave. A perfect electric conductor (PEC) ring is placed between the RCP source and the metasurface to limit the area of incidence to the circular metasurface region. Figure 4a–c are the intensity profiles of  $x$ - $z$  cross sections for  $l = 1, 2, 3$ , respectively, and the white dashed line marks the position of the focal-plane ( $z = 10.0\ \mu\text{m}$ ). There is a small deviation ( $<1\%$ ) between the simulated focal length and the designed focal length. The deviation can be attributed to the discrete phase of each meta-atom for an approximation of the continuous phase distribution. Figure 4d–f demonstrate the donut-shaped focal spot on the focal plane. It can be observed that the minimum intensity of the vortex ring is at the center of the focal plane. The bottom-left insets of Figure 4d–f show corresponding phase patterns at the focal plane. It illustrates that, as the topological charge  $l$  increases, the number of spirals in the phase pattern also increases. Figure 4g–i demonstrate the corresponding horizontal cuts of focal spots. The full widths at half maximum (FWHM) of horizontal cuts of the optical vortex ring are 311 nm, 335 nm, and 355 nm, respectively. The efficiencies of the FOV are as high as 75.1% (for  $l = 1$ ), 73.0% (for  $l = 2$ ), and 71.0% (for  $l = 3$ ). Here, the efficiency of the FOV is defined as the ratio of the transmitted power passing through the focal spot in a circle whose radius is three times the FWHM. The definition of the FOV's efficiency is the same as in [36]. The focusing efficiency decreases as the topological charge increases, mainly due to the increase in the vortex ring's diameter.

The FWHM of horizontal cuts of vortex rings and focusing efficiencies are calculated under a different NA in Figure 5. The radius of all the designed metasurfaces is  $6\ \mu\text{m}$ , and the topological charge  $l$  is kept at 1. It can be seen that, as NA increases, both FWHM and focusing efficiency are decreased, which can also be attributed to the decrease in the vortex ring's diameter. All the metasurfaces were diffraction limited ( $\text{FWHM} < \lambda/(2\text{NA})$ ). The maximum value of NA reaches 0.788, and the maximum of focusing efficiency is measured to be as high as 79.2%. As far as we are concerned, the focusing efficiency seems to be promising compared to prior work [37–40].

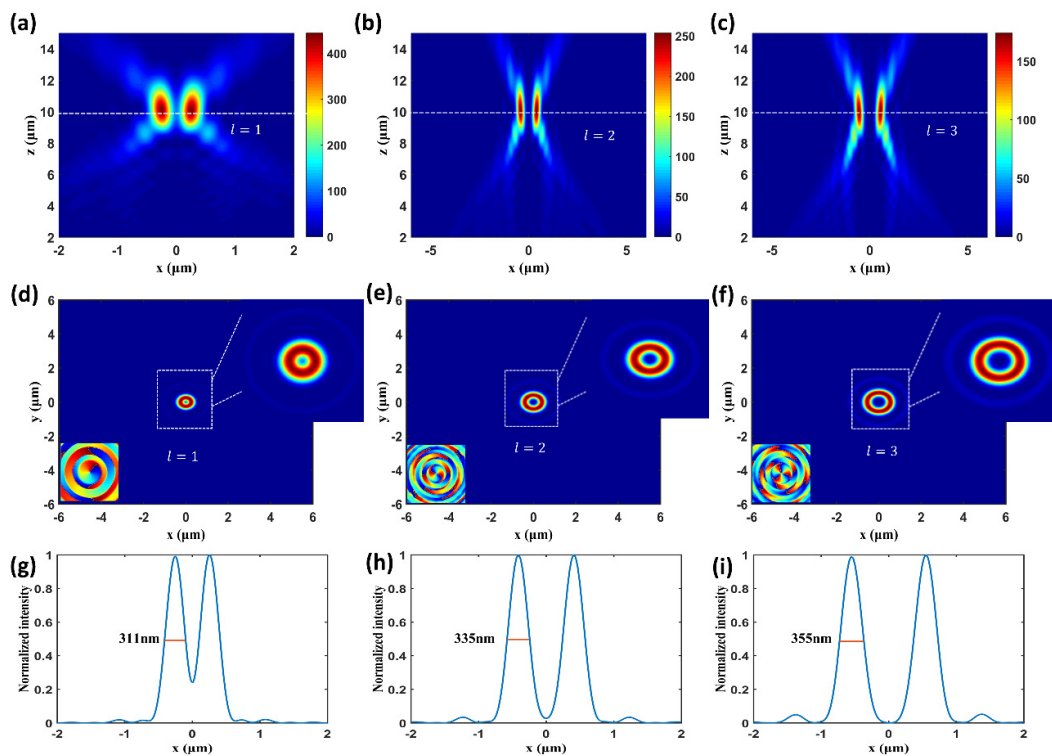


**Figure 4.** Numerically simulated results for a focused optical vortex (FOV) generator. Electric field intensity profile in  $xz$ -plane for (a)  $l = 1$ , (b)  $l = 2$ , and (c)  $l = 3$ . The white dashed line denotes the focal plane. The vortex rings are imaged at the focal plane,  $z = 10 \mu\text{m}$ , along with their phase pattern in the corresponding bottom-left inset figure for (d)  $l = 1$ , (e)  $l = 2$ , (f)  $l = 3$  in  $xy$ -plane, (a,d), (b,e), and (c,f) share the same color bars, respectively. The upper-right inset maps show the amplification of the vortex ring. (g–i) The corresponding horizontal cuts of vortex rings at the focal spot having a full width half maximum (FWHM) of 311 nm, 335 nm, and 355 nm, respectively.

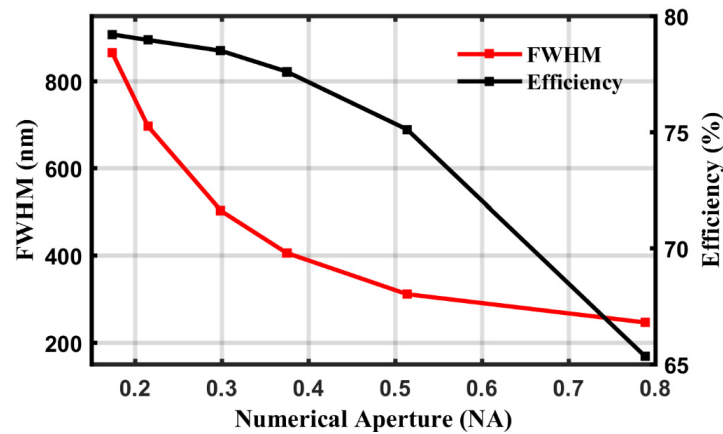


**Figure 5.** The FWHM of horizontal cuts of vortex rings and focusing efficiencies versus NA of the FOV generators under an RCP wave incidence of 355 nm. The radius of the metasurface is kept at  $6 \mu\text{m}$  and the topological charge  $l$  of the OV is kept at 1.

### 3.2. Multichannel FOV Generation and Detection

A transmission-mode multichannel FOV (MCFOV) generator design principle based on metasurfaces is demonstrated. The phase distribution profile  $\phi_m(x, y)$  of the MCFOV generator of the  $x$ - $y$  cross section at  $z = 0$  is the synthetic phase of the multiple FOV beam interference.

$$\phi_m(x, y) = \text{arg}\left(\sum_{i=1}^n E_i(x, y)e^{j\varphi_i}\right) \quad (5)$$

$$\theta(x, y) = \phi_m(x, y)/2 \quad (6)$$

where

$$\varphi_i(x, y) = -\frac{2\pi}{\lambda}\left(\sqrt{(x-x_i)^2+(y-y_i)^2+f^2}-\sqrt{x_i^2+y_i^2+f^2}\right)+l_i\times\arctan\left(\frac{y}{x}\right) \quad (7)$$

Here,  $E_i(x, y)$  is the amplitude distribution of the  $i^{\text{th}}$  targeted beam,  $\varphi_i$  is the phase profile of the  $i^{\text{th}}$  targeted beam, where these two factors determine the intensity distribution of the transmitted light beam in the focal plane,  $l_i$  is the topological charge number of the  $i^{\text{th}}$  targeted beam,  $f$  is the distance between the metasurface and the focal plane,  $(x_i, y_i)$  is the  $i^{\text{th}}$  designed coordinate of the focal spot in the focal plane, and  $n$  is the total number of the targeted beam. It is worth mentioning that if the metasurface is large enough, both  $n$  and  $|l|$  can be any arbitrary large positive integer. Here, for simplicity, we assume that  $n = 5$ ,  $E_i = \sqrt{1/n}$ , and  $l = [-2, -1, 0, 1, 2]$ . Through adjusting the rotation angle  $\theta(x, y)$  of optimized nanobars on the metasurface, the design of the MCFOV can be obtained.

As schematically depicted in Figure 6a, the elaborately designed metasurface with a radius of  $6 \mu\text{m}$  can generate five-channel FOV beams with topological charges from  $-2$  to  $2$  under the RCP plane wave incidence at  $355 \text{ nm}$ . The corresponding focal spots are generated on the focal plane  $10 \mu\text{m}$  away from the metasurface. The simulated result of the multichannel FOV generator is shown in Figure 6a. The topological charges change from  $-2$  to  $2$ , and the corresponding focal spots are located at  $(0, -3 \mu\text{m})$ ,  $(-3 \mu\text{m}, 0)$ ,  $(0, 0)$ ,  $(3 \mu\text{m}, 0)$ ,  $(0, 3 \mu\text{m})$  on the focal plane, respectively. This device can realize a high efficiency of over  $12\%$  in every channel, which is much higher than the previous work [39].

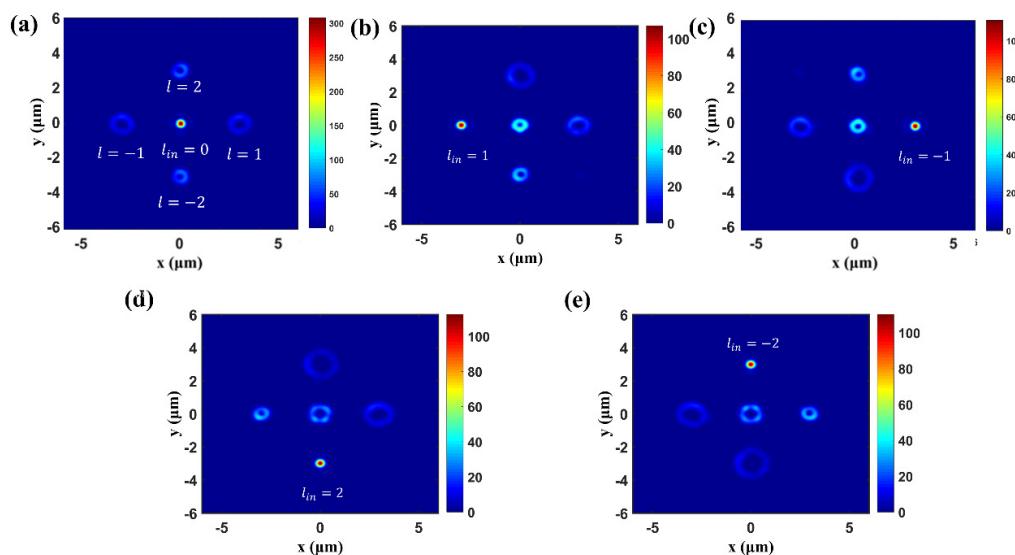


**Figure 6.** Numerical simulated result of a multichannel FOV generator operating in transmission mode. (a) The RCP incident wave illuminates the generator along the positive  $z$ -axis and divides into five FOV beams with different orbital angular momentum (OAM) values. (b–e) The incident waves with different topological charge numbers of (b)  $l = 1$ , (c)  $l = -1$ , (d)  $l = 2$ , and (e)  $l = -2$  illuminate the generator. (b–e) The corresponding intensity profiles on the focal plane at  $z = 10 \mu\text{m}$

Besides, the designed metasurface is capable of interacting with incident OV beams. These OV beams can be obtained by a traditional OV generator [8] and a metasurface. When the OV beam with topological charge  $l = l_{in}$ , illustrated in the metasurface mentioned above, the transmitted beam carries the orbital angular momentum (OAM)  $l_{out}\hbar = (l_{in} + l_i)\hbar$ , where  $\hbar$  is the reduced Planck's constant. The annihilation of the OAM occurs when  $l_{out}$  equals zero, resulting in a solid spot on the focal plane. One can identify the OAM of the incidence by recognizing the solid spot's position according to the metasurface design. For better understanding, the previously designed metasurface is illuminated by normal incident RCP OV beams (RCP plane wave with a phase evolution in the form of  $e^{il\theta}$ ) with different topological charges from  $-2$  to  $2$  and the corresponding simulation results are shown in Figure 6b–e, respectively. It is necessary to mention that an optical vortex with a larger topological charge can be identified with more sizeable metasurfaces.

#### 4. Conclusions

In summary, an ultra-thin, highly efficient all-dielectric metasurface is demonstrated for FOV generation and optical vortex detection. The all-dielectric metasurface comprises Nb<sub>2</sub>O<sub>5</sub> nanobars on a silica substrate. The meta-atom operates as a miniature half-wave plate with a cross-polarized efficiency of 86.9%. This high efficiency is achieved due to the existence of both electric and magnetic resonance in the nanobar. A phase delay of  $\pi$  between the  $x$ - and  $y$ -polarized electric field components is attributed to the different parity of the numbers of AMDs induced by the incident light. Based on this concept, we demonstrate the FOV generation with distinct topological charges and NA. The designed FOV generator shows a maximum efficiency of 79.2%. Moreover, a multichannel device which can simultaneously generate and detect the OV beams with varying OAMs in a single metasurface has been demonstrated in the UV range. We envision that our designed devices of high flexibility and ultra-thin thickness may have potential use in high-performance micron-scale integrated ultraviolet nanophotonics and meta-optics.

**Author Contributions:** Conceptualization, Z.Z.; Data curation, Z.Z.; Formal analysis, Z.Z.; Funding acquisition, G.S.; Visualization, Z.Z.; Investigation Z.Z.; Writing, original draft preparation, Z.Z.; Writing-original draft, Z.Z.; Writing, review, and editing, Z.Z., T.L., and X.J.; supervision, G.S. and Y.X. All of the authors discussed the results and commented on the manuscript. All authors have read and agreed to the published version of the manuscript.

**Funding:** The project was supported by the Strategic Priority Research Program of the Chinese Academy of Sciences, Grant No. XDB43010000, the National Key Research and Development Plan (No.2016YFB0400601 and No.2016YFB0402402), the National Basic Research Program of China (973 Program) (No. 2015CB351902), the National Science and Technology Major Project (2018ZX01005101-010), the National Natural Science Foundation of China (Grant No. 61835011 and Grant No. U1431231) the Key Research Projects of the Frontier Science of the Chinese Academy of Sciences (No. QYZDY-SSW-JSC004), and the Beijing Science and Technology Projects (Grant No. Z151100001615042).

**Conflicts of Interest:** The authors declare no competing interests.

#### References

- Allen, L.; Beijersbergen, M.W.; Spreeuw, R.J.; Woerdman, J.P. Orbital angular momentum of light and the transformation of Laguerre-Gaussian laser modes. *Phys. Rev. A* **1992**, *45*, 8185–8189. [[CrossRef](#)]
- Zhang, Y.; Shi, W.; Shen, Z.; Man, Z.; Min, C.; Shen, J.; Zhu, S.; Urbach, H.P.; Yuan, X. A Plasmonic Spanner for Metal Particle Manipulation. *Sci. Rep.* **2015**, *5*, 15446. [[CrossRef](#)]
- Zhang, Y.; Shen, J.; Min, C.; Jin, Y.; Jiang, Y.; Liu, J.; Zhu, S.; Sheng, Y.; Zayats, A.V.; Yuan, X. Nonlinearity-Induced Multiplexed Optical Trapping and Manipulation with Femtosecond Vector Beams. *Nano Lett.* **2018**, *18*, 5538–5543. [[CrossRef](#)]
- Toninelli, E.; Ndagano, B.; Vallés, A.; Sephton, B.; Nape, I.; Ambrosio, A.; Capasso, F.; Padgett, M.J.; Forbes, A. Concepts in quantum state tomography and classical implementation with intense light: A tutorial. *Adv. Opt. Photonics* **2019**, *11*. [[CrossRef](#)]
- Chen, Y.; Gao, J.; Jiao, Z.Q.; Sun, K.; Shen, W.G.; Qiao, L.F.; Tang, H.; Lin, X.F.; Jin, X.M. Mapping Twisted Light into and out of a Photonic Chip. *Phys. Rev. Lett.* **2018**, *121*, 233602. [[CrossRef](#)]

6. Jeffries, G.D.M.; Edgar, J.S.; Zhao, Y.; Shelby, J.P.; Fong, C.; Chiu, D.T. Using Polarization-Shaped Optical Vortex Traps for Single-Cell Nanosurgery. *Nano Lett.* **2007**, *7*, 415–420. [[CrossRef](#)] [[PubMed](#)]
7. Karabchevsky, A. On-chip optical vortex-based nanophotonic detectors. *Light Sci. Appl.* **2020**, *9*, 115. [[CrossRef](#)] [[PubMed](#)]
8. Sueda, K.; Miyaji, G.; Miyanaga, N.; Nakatsuka, M. Laguerre-Gaussian beam generated with a multilevel spiral phase plate for high intensity laser pulses. *Opt. Express* **2004**, *12*, 3548–3553. [[CrossRef](#)] [[PubMed](#)]
9. Padgett, M.; Allen, L. Orbital angular momentum exchange in cylindrical-lens mode converters. *J. Opt. B Quantum Semiclass Opt.* **2002**, *4*, S17. [[CrossRef](#)]
10. Beijersbergen, M.W.; Allen, L.; van der Veen, H.E.L.O.; Woerdman, J.P. Astigmatic laser mode converters and transfer of orbital angular momentum. *Opt. Commun.* **1993**, *96*, 123–132. [[CrossRef](#)]
11. Yu, N.; Genevet, P.; Kats, M.A.; Aieta, F.; Tetienne, J.P.; Capasso, F.; Gaburro, Z. Light propagation with phase discontinuities: Generalized laws of reflection and refraction. *Science* **2011**, *334*, 333–337. [[CrossRef](#)] [[PubMed](#)]
12. Yu, N.; Aieta, F.; Genevet, P.; Kats, M.A.; Gaburro, Z.; Capasso, F. A broadband, background-free quarter-wave plate based on plasmonic metasurfaces. *Nano Lett.* **2012**, *12*, 6328–6333. [[CrossRef](#)] [[PubMed](#)]
13. Luo, X.; Hu, Y.; Li, X.; Jiang, Y.; Wang, Y.; Dai, P.; Liu, Q.; Shu, Z.; Duan, H.J.A.O.M. Integrated Metasurfaces with Microprints and Helicity-Multiplexed Holograms for Real-Time Optical Encryption. *Adv. Opt. Mater.* **2020**, *8*, 1902020. [[CrossRef](#)]
14. Zheng, G.; Muhlenbernd, H.; Kenney, M.; Li, G.; Zentgraf, T.; Zhang, S. Metasurface holograms reaching 80% efficiency. *Nat. Nanotechnol.* **2015**, *10*, 308–312. [[CrossRef](#)] [[PubMed](#)]
15. Avrahamy, R.; Zohar, M.; Auslender, M.; Milgrom, B.; Hava, S.; Shikler, R. In-depth investigation and applications of novel silicon photonics microstructures supporting optical vorticity and waveguiding for ultra-narrowband near-infrared perfect absorption. *Photonics Res.* **2020**, *8*, 381–394. [[CrossRef](#)]
16. Chen, D.C.; Zhu, X.F.; Wu, D.J.; Liu, X.J. Broadband Airy-like beams by coded acoustic metasurfaces. *Appl. Phys. Lett.* **2019**, *114*. [[CrossRef](#)]
17. Jin, R.; Tang, L.; Li, J.; Wang, J.; Wang, Q.; Liu, Y.; Dong, Z.G. Experimental Demonstration of Multidimensional and Multifunctional Metalenses Based on Photonic Spin Hall Effect. *ACS Photonics* **2020**, *7*, 512–518. [[CrossRef](#)]
18. Avayu, O.; Almeida, E.; Prior, Y.; Ellenbogen, T. Composite functional metasurfaces for multispectral achromatic optics. *Nat. Commun.* **2017**, *8*, 14992. [[CrossRef](#)]
19. Zhang, L.; Ding, J.; Zheng, H.; An, S.; Lin, H.; Zheng, B.; Du, Q.; Yin, G.; Michon, J.; Zhang, Y.; et al. Ultra-thin high-efficiency mid-infrared transmissive Huygens meta-optics. *Nat. Commun.* **2018**, *9*, 1481. [[CrossRef](#)]
20. Zhang, S.; Soibel, A.; Keo, S.A.; Wilson, D.; Rafol, S.B.; Ting, D.Z.; She, A.; Gunapala, S.D.; Capasso, F. Solid-immersion metalenses for infrared focal plane arrays. *Appl. Phys. Lett.* **2018**, *113*. [[CrossRef](#)]
21. Vo, S.; Fattal, D.; Sorin, W.V.; Peng, Z.; Tran, T.; Fiorentino, M.; Beausoleil, R.G. Sub-Wavelength Grating Lenses With a Twist. *IEEE Photonics Technol. Lett.* **2014**, *26*, 1375–1378. [[CrossRef](#)]
22. Khorasaninejad, M.; Zhu, A.Y.; Roques-Carmes, C.; Chen, W.T.; Oh, J.; Mishra, I.; Devlin, R.C.; Capasso, F. Polarization-Insensitive Metalenses at Visible Wavelengths. *Nano Lett.* **2016**, *16*, 7229–7234. [[CrossRef](#)] [[PubMed](#)]
23. Wang, S.; Wu, P.C.; Su, V.C.; Lai, Y.C.; Chen, M.K.; Kuo, H.Y.; Chen, B.H.; Chen, Y.H.; Huang, T.T.; Wang, J.H.; et al. A broadband achromatic metalens in the visible. *Nat. Nanotechnol.* **2018**, *13*, 227–232. [[CrossRef](#)] [[PubMed](#)]
24. Fan, Z.B.; Shao, Z.K.; Xie, M.Y.; Pang, X.N.; Ruan, W.S.; Zhao, F.L.; Chen, Y.J.; Yu, S.Y.; Dong, J.W. Silicon Nitride Metalenses for Close-to-One Numerical Aperture and Wide-Angle Visible Imaging. *Phys. Rev. Appl.* **2018**, *10*, 014005. [[CrossRef](#)]
25. Deng, Y.; Wang, X.; Gong, Z.; Dong, K.; Lou, S.; Pegard, N.; Tom, K.B.; Yang, F.; You, Z.; Waller, L.; et al. All-Silicon Broadband Ultraviolet Metasurfaces. *Adv. Mater.* **2018**, *30*, e1802632. [[CrossRef](#)]
26. Zhang, C.; Divitt, S.; Fan, Q.; Zhu, W.; Agrawal, A.; Lu, Y.; Xu, T.; Lezec, H.J. Low-loss metasurface optics down to the deep ultraviolet region. *Light Sci. Appl.* **2020**, *9*, 55. [[CrossRef](#)]
27. Gao, X.; Wan, R.; Yan, J.; Wang, L.; Yi, X.; Wang, J.; Zhu, W.; Li, J. Design of AlN ultraviolet metasurface for single-/multi-plane holography. *Appl. Opt.* **2020**, *59*, 4398–4403. [[CrossRef](#)]
28. Rani, R.A.; Zoofakar, A.S.; O'Mullane, A.P.; Austin, M.W.; Kalantar-Zadeh, K. Thin films and nanostructures of niobium pentoxide: Fundamental properties, synthesis methods and applications. *J. Mater. Chem. A* **2014**, *2*, 15683–15703. [[CrossRef](#)]

29. Hota, M.K.; Bera, M.K.; Maiti, C.K. Flexible metal–insulator–metal capacitors on polyethylene terephthalate plastic substrates. *Semicond. Sci. Technol.* **2012**, *27*. [[CrossRef](#)]
30. Menzel, C.; Rockstuhl, C.; Lederer, F. Advanced Jones calculus for the classification of periodic metamaterials. *Phys. Rev. A* **2010**, *82*. [[CrossRef](#)]
31. Kang, M.; Feng, T.; Wang, H.T.; Li, J. Wave front engineering from an array of thin aperture antennas. *Opt. Express* **2012**, *20*, 15882–15890. [[CrossRef](#)] [[PubMed](#)]
32. Gao, L.; Lemarchand, F.; Lequime, M.J.O.e. Exploitation of multiple incidences spectrometric measurements for thin film reverse engineering. *Opt. Express* **2012**, *20*, 15734–15751. [[CrossRef](#)] [[PubMed](#)]
33. Palik, E.D. *Handbook of Optical Constants of Solids*; Academic Press: Cambridge, MA, USA, 1998; Volume 3.
34. Luo, W.; Sun, S.; Xu, H.X.; He, Q.; Zhou, L. Transmissive Ultrathin Pancharatnam-Berry Metasurfaces with nearly 100% Efficiency. *Phys. Rev. Appl.* **2017**, *7*. [[CrossRef](#)]
35. Huang, K.; Deng, J.; Leong, H.S.; Yap, S.L.K.; Yang, R.B.; Teng, J.; Liu, H. Ultraviolet Metasurfaces of  $\approx 80\%$  Efficiency with Antiferromagnetic Resonances for Optical Vectorial Anti-Counterfeiting. *Laser Photonics Rev.* **2019**, *13*. [[CrossRef](#)]
36. Arbabi, A.; Horie, Y.; Ball, A.J.; Bagheri, M.; Faraon, A. Subwavelength-thick lenses with high numerical apertures and large efficiency based on high-contrast transmitarrays. *Nat. Commun.* **2015**, *6*, 7069. [[CrossRef](#)]
37. Ahmed, H.; Rahim, A.A.; Maab, H.; Ali, M.M.; Mahmood, N.; Naureen, S. Phase engineering with all-dielectric metasurfaces for focused-optical-vortex (FOV) beams with high cross-polarization efficiency. *Opt. Mater. Express* **2020**, *10*. [[CrossRef](#)]
38. Mahmood, N.; Kim, I.; Mehmood, M.Q.; Jeong, H.; Akbar, A.; Lee, D.; Saleem, M.; Zubair, M.; Anwar, M.S.; Tahir, F.A.; et al. Polarisation insensitive multifunctional metasurfaces based on all-dielectric nanowaveguides. *Nanoscale* **2018**, *10*, 18323–18330. [[CrossRef](#)]
39. Jin, J.; Pu, M.; Wang, Y.; Li, X.; Ma, X.; Luo, J.; Zhao, Z.; Gao, P.; Luo, X. Multi-Channel Vortex Beam Generation by Simultaneous Amplitude and Phase Modulation with Two-Dimensional Metamaterial. *Adv. Mater. Technol.* **2017**, *2*. [[CrossRef](#)]
40. Kanwal, S.; Wen, J.; Yu, B.; Kumar, D.; Chen, X.; Kang, Y.; Bai, C.; Zhang, D. High-Efficiency, Broadband, Near Diffraction-Limited, Dielectric Metalens in Ultraviolet Spectrum. *Nanomaterials* **2020**, *10*, 490. [[CrossRef](#)]



© 2020 by the authors. Licensee MDPI, Basel, Switzerland. This article is an open access article distributed under the terms and conditions of the Creative Commons Attribution (CC BY) license (<http://creativecommons.org/licenses/by/4.0/>).